Sun *et al. Soft Sci.* **2025**, *5*, 35
DOI: 10.20517/ss.2025.21

Soft Science

Research Article

Open Access

Check for updates

Dielectric shell regulation in synergy FeCoNi@$ZnIn_2S_4$ microspheres with broadband electromagnetic wave absorption

Rui Sun[1], Huwei Lv[1], Gangjie Lian[2], Lei Wang[3,*], Mengqiu Huang[4], Wenbin You[4], Renchao Che[1,2,4,*]

[1]School of Physics and Materials Science, Nanchang University, Nanchang 330031, Jiangxi, China.
[2]International Institute for Materials Innovation, Nanchang University, Nanchang 330031, Jiangxi, China.
[3]School of Materials Science and Engineering, Tongji University, Shanghai 201804, China.
[4]Laboratory of Advanced Materials, Shanghai Key Lab of Molecular Catalysis and Innovative Materials, State Key Laboratory of Coatings for Advanced Equipment, College of Smart Materials and Future Energy, Fudan University, Shanghai 200438, China.

[*]**Correspondence to:** Prof. Renchao Che, School of Physics and Materials Science, Nanchang University, No. 999 Xuefu Road, Honggutan District, Nanchang 330031, Jiangxi, China. E-mail: rcche@fudan.edu.cn; Dr. Lei Wang, School of Materials Science and Engineering, Tongji University, No. 4800 Caoan Road, Jiading District, Shanghai 201804, China. E-mail: lei_wang@tongji.edu.cn

How to cite this article: Sun, R.; Lv, H.; Lian, G.; Wang, L.; Huang, M.; You, W.; Che, R. Dielectric shell regulation in synergy FeCoNi@$ZnIn_2S_4$ microspheres with broadband electromagnetic wave absorption. *Soft Sci.* **2025**, *5*, 35. https://dx.doi.org/10.20517/ss.2025.21

Received: 28 May 2025 **First Decision:** 13 Jun 2025 **Revised:** 8 Jul 2025 **Accepted:** 10 Jul 2025 **Published:** 18 Jul 2025

Academic Editor: Guanglei Wu **Copy Editor:** Pei-Yun Wang **Production Editor:** Pei-Yun Wang

Abstract

Core-shell structure and magnetic-dielectric coupling in functional composites are important factors for obtaining excellent electromagnetic (EM) wave absorption performance, but they also face challenges. In this study, magnetic FeCoNi and dielectric $ZnIn_2S_4$ were combined to form unique core-shell structured microspheres. The morphology characteristics, EM parameters, and absorption performance of FeCoNi@$ZnIn_2S_4$ composites with different annealing temperatures were investigated to reveal impedance matching and synergistic absorption mechanisms. Those results show that FeCoNi@$ZnIn_2S_4$-600 (FCNZ-600) has excellent EM wave absorption properties, with the minimum reflection loss (RL_{min}) of -52.4 dB at 1.9 mm and the efficient absorption bandwidth of 6.08 GHz at 1.53 mm, which achieves broadband absorption. Core-shell magnetic-dielectric design provides a new perspective in efficient EM wave absorption systems.

Keywords: Core-shell, FeCoNi@$ZnIn_2S_4$, high broadband, electromagnetic wave absorption

INTRODUCTION

Recently, the progress of modern electronic and wireless communication technologies is generating excellent electromagnetic (EM) radiation, resulting in significant pollution that disrupts the functionality of electronic systems and poses substantial risks to human health and ecological stability[1-6]. As a result, EM wave absorption materials have become a research hotspot with particular emphasis on achieving efficient broadband absorption, which remains a critical challenge in the field[7-10].

Among those diverse EM wave absorption materials, magnetic-dielectric synergistic composites integrate the benefits of both magnetic and dielectric components to achieve superior absorption performance[11,12]. The magnetic component induces magnetic loss, while the dielectric component contributes to dielectric loss[13-15]. The synergistic magnetic-dielectric effect has enabled multiple loss mechanisms, thereby significantly enhancing the material's EM wave attenuation capacity and achieving a more effective absorption outcome[16,17].

Core-shell EM wave absorption materials with specialized heterojunction interfaces offer distinct advantages, providing a synergistic loss effect to dissipate the incident energy[18,19]. This interface features unique electronic structures and physicochemical properties that generate various specific response behavior, thereby broadening the effective absorption bandwidth[20,21]. Core-shell structured materials present novel strategies in advanced EM wave absorption. Numerous studies have documented that the core-shell magnetic-dielectric composites with enhanced absorption performance, integrating magnetic materials (alloys, Fe_3O_4, ferrites, and MOFs-derivatives) with dielectric components of choice, including transition metal sulfides, carbides, and polymers, such as CoFe@C@C[22], CNC/Fe_3O_4@C[23], $ZnFe_2O_4$ @PPy[24], and $CoFe_2O_4$@Fe_3C@NiO[25].

In this study, magnetic FeCoNi and dielectric $ZnIn_2S_4$ were combined to construct core-shell structured microspheres with magnetic-dielectric synergy, utilizing chemical reduction, oil bath, and in-situ annealing techniques to achieve tunable EM properties. The selection of magnetic components focused on FeCoNi alloys, which are well-known magnetic materials with high saturation magnetization and permeability, leading to significant magnetic loss and a strong magnetic response to EM wave[26]. In contrast, the choice of dielectric shell components has predominantly centered on binary transition metal sulfides, such as MoS_2[27], CuS[28], and NiS_2[29], while research on ternary metal sulfide EM wave absorption materials remains limited. As a result, there are considerable challenges and opportunities for advancement in this domain. $ZnIn_2S_4$, a representative ternary metal sulfide, has been extensively investigated in the field of photocatalysis due to its unique photoelectric properties, low toxicity, good chemical stability, and semiconductor characteristics, making it an appealing candidate for further exploration in EM wave absorption[30]. $ZnIn_2S_4$ has the advantage of being able to enhance the polarization intensity through phase regulation and the introduction of crystal defects. Meanwhile, the band gap of $ZnIn_2S_4$ (2.4-2.6 eV[31]) lies between that of $CdIn_2S_4$ (2.0-2.37 eV[32]) and $ZnGa_2S_4$ (3.18 eV[33]), possessing moderate conductivity and dielectric loss capability. Despite $ZnIn_2S_4$ having relatively low conductivity[34], its combination with FeCoNi in a core-shell structure allows the conductive channels of FeCoNi to penetrate $ZnIn_2S_4$, thereby enhancing internal charge transfer. Moreover, the interface formed between these components plays a crucial role in enhancing conductivity, ultimately optimizing EM wave absorption performance. Thus, this work presents FeCoNi@$ZnIn_2S_4$ composites, leveraging synergistic core-shell composites to overcome challenges in achieving efficient and tunable absorption.

EXPERIMENTAL

Chemicals and reagents

Ferrous sulfate ($FeSO_4·7H_2O$), zinc chloride ($ZnCl_2$), thioacetamide (C_2H_5NS), sodium hydroxide (NaOH), glycerol ($C_3H_8O_3$) and hydrazine hydrate ($N_2H_4·H_2O$) were purchased from Sinopharm Chemical Reagent Co., Ltd., cobalt (II) chloride hexahydrate ($CoCl_2·6H_2O$), nickel (II) chloride hexahydrate ($NiCl_2·6H_2O$), were got from Shanghai Aladdin Biochemical Technology Co., Ltd., Indium (III) chloride tetrahydrate ($InCl_3·4H_2O$) was got from Shanghai Macklin Biochemical Technology Co., Ltd.

Preparation of FeCoNi microspheres

The FeCoNi microspheres were synthesized at room temperature. Firstly, 1.668 g $FeSO_4·7H_2O$, 1.142 g $CoCl_2·6H_2O$, and 0.285 g $NiCl_2·6H_2O$ were all dissolved in 100 mL H_2O with stirring 3 min (solution A). After that, 5 g NaOH and 18 mL $N_2H_4·H_2O$ were dissolved in 10 mL H_2O (solution B). Then, solution B was slowly added drop by drop to solution A. After reacting 24 h, the final FeCoNi microspheres were magnetically separated and further washed with H_2O and EtOH several times, and dried under vacuum in an oven at 60 °C overnight.

Preparation of FeCoNi@$ZnIn_2S_4$ microspheres

The original FeCoNi@$ZnIn_2S_4$ microspheres were synthesized by oil bath method. Firstly, 0.027 g $ZnCl_2$, 0.117 g $InCl_3·4H_2O$ and 0.060 g C_2H_5NS were dissolved in 80 mL H_2O and 20 mL glycerol with vigorous stirring for 30 min, after which 0.2 g FeCoNi microspheres powders were poured into the above mixture to be ultrasonicated for 10 min. Then, the mixture was heated at 80 °C for 2 h, cooled down to room temperature and then washed with H_2O and EtoH for several times. Finally, the original FeCoNi@$ZnIn_2S_4$ microspheres were dried at 60 °C overnight. The original FeCoNi@$ZnIn_2S_4$ microspheres were denoted as FCNZ. $ZnIn_2S_4$ can also be prepared by using the above procedures without the addition of FeCoNi.

To obtain the final FeCoNi@$ZnIn_2S_4$-500, FeCoNi@$ZnIn_2S_4$-600 and FeCoNi@$ZnIn_2S_4$-700 microspheres, the FeCoNi@$ZnIn_2S_4$ powders were annealed in H_2/Ar at 500, 600, and 700 °C for 5 h. The FeCoNi@$ZnIn_2S_4$-500, FeCoNi@$ZnIn_2S_4$-600 and FeCoNi@$ZnIn_2S_4$-700 microspheres were denoted as FCNZ-500, FCNZ-600 and FCNZ-700. $ZnIn_2S_4$ was annealed under the identical conditions to obtain the $ZnIn_2S_4$-500, $ZnIn_2S_4$-600, and $ZnIn_2S_4$-700.

Characterization and measurement

The crystal structure of the samples was analyzed by X-ray diffraction (XRD, Brucker, D8 ADVANCED). The morphology of the samples was observed using field emission scanning electron microscope (FESEM, HITACHI, S4800). The JEOL JEM-2100F transmission electron microscope (TEM) was used to analyze the material morphology. The XPS spectra in this study were obtained using a Thermo Scientific ESCALAB 250Xi. The hysteresis loops were analyzed using a superconducting quantum interference device magnetometer [MPMS(SQUID) VSM]. The mixtures of $ZnIn_2S_4$, FeCoNi, $ZnIn_2S_4$-500, $ZnIn_2S_4$-600, $ZnIn_2S_4$-700, FCNZ, FCNZ-500, FCNZ-600, and FCNZ-700 composites with 60 wt% paraffin were measured by using the Agilent N5230C vector network analyzer over the range of 2-18 GHz. Detailed information can be found in the Supplementary Materials.

RESULT AND DISCUSSION

Structural and morphology analysis

The synthesis process and morphological evolution of FCNZ-500, FCNZ-600 and FCNZ-700 microspheres are depicted in Figure 1A. Firstly, metal salt ions (Fe^{2+}, Co^{2+}, and Ni^{2+}) were combined with OH^-, and subsequently ferromagnetic FeCoNi powders were synthesized in the presence of hydrazine hydrate ($N_2H_4·H_2O$). Next, it was ultrasonically dispersed in a mixed solution of glycerol and water containing Zn^{2+},

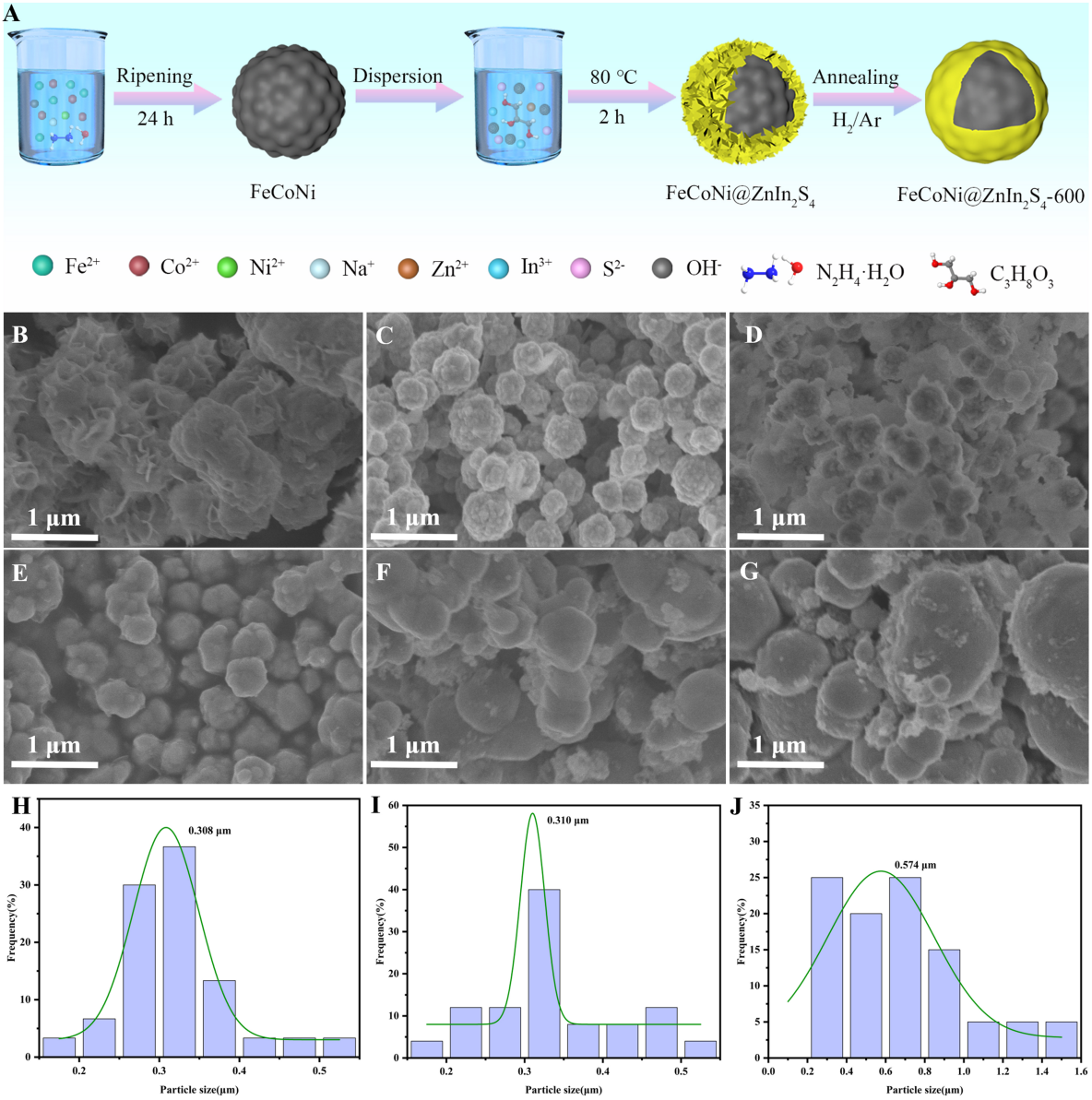

Figure 1. (A) Schematic synthesis of annealed FeCoNi@$ZnIn_2S_4$ microspheres with core-shell structure; SEM images of (B) $ZnIn_2S_4$, (C) FeCoNi, (D) FeCoNi@$ZnIn_2S_4$, (E) FCNZ-500, (F) FCNZ-600 and (G) FCNZ-700 microspheres; the particle size distribution of (H) FCNZ-500, (I) FCNZ-600 and (J) FCNZ-700 microspheres. SEM: Scanning electron microscope.

In^{3+}, and S^{2-} and then heated by an oil bath for 2 h. The $ZnIn_2S_4$ nanosheets as a dielectric shell were grown on FeCoNi microspheres and subsequently annealed at different temperatures.

The resulting SEM images are displayed in Figure 1B-G. Pure $ZnIn_2S_4$ is a flower-like microsphere assembled from numerous irregular nanosheets. Different diameters and sizes of flower-like microspheres can be seen inside the cluster[35]. Subsequently, $ZnIn_2S_4$ nanosheets were grown on the rough FeCoNi microspheres, which indicates the core-shell FCNZ structure. At the same time, as the annealing temperature increased, the microspheres gradually became smoother, and the average particle size gradually increased [Figure 1H-J].

Subsequently, the microstructure and internal composition of the FCNZ-500, FCNZ-600, and FCNZ-700 were further analyzed. Figure 2A-C respectively represents the TEM images of FCNZ-500, FCNZ-600, and FCNZ-700. As the annealing temperature ascends from 500 to 600 °C, the interfacial bonding degree in the $ZnIn_2S_4$-FeCoNi region in FCNZ-600 was enhanced. However, when the temperature further rose to 700 °C, the crystal structure of $ZnIn_2S_4$ in FCNZ-700 might be optimized to some extent, but the nanosheets tend to agglomerate and the structural uniformity decreases. This phenomenon is also in accordance with the corresponding permittivity results. High resolution transmission electron microscopy (HRTEM) and the corresponding fast Fourier transform (FFT) patterns [Figure 2D-G] further validate that the FCNZ-600 composite material is composed of FeCoNi and $ZnIn_2S_4$. By measuring the lattice spacing, 0.223 nm corresponded to the (110) FeCoNi [Figure 2G and G(i)][36], while 0.337 and 0.196 nm corresponded to the (101) and (110) $ZnIn_2S_4$ [Figure 2E, E(i), and E(ii)][37]. Simultaneously, two lattice spacings, 0.342 and 0.218 nm, were identified at the core-shell interface, corresponding to the (101) plane of $ZnIn_2S_4$ and the (110) plane of FeCoNi [Figure 2F, F(i), and F(ii)], respectively. These results further confirm that the structure of FCNZ-600 constitutes a hybrid system featuring a tight interface contact. The high-angle annular dark-field (HAADF) image [Figure 2H] and energy-dispersive X-ray spectroscopy (EDS) spectra [Supplementary Figure 1] show that Fe, Co, and Ni elements focus in spherical center, while Zn, In, and S elements are displayed in the shell region. During high-temperature annealing, the thermal motion of atoms intensifies, providing sufficient energy to drive diffusion across phase boundaries. As a result, Fe, Co, and Ni elements diffuse from the FeCoNi core to the $ZnIn_2S_4$ shell. This diffusion leads to the formation of a gradient interface, thereby optimizing electronic transport and polarization behavior at the interface.

Figure 3A displays the diffraction patterns of $ZnIn_2S_4$ annealed at 500, 600, and 700 °C. With increasing annealing temperature, the crystallinity of the material becomes progressively more defined and pronounced. The $ZnIn_2S_4$ sample annealed at 700 °C corresponds to two standard reference patterns, PDF#72-1445 and PDF#65-2023. As shown in Figure 3B, FCNZ-500, FCNZ-600, and FCNZ-700 exhibit three prominent diffraction peaks at (110), (200), and (211), which are attributed to the face-centered cubic (FCC) structure[26]. However, due to the weak intensity of the $ZnIn_2S_4$ diffraction peak [Supplementary Figure 2], the corresponding diffraction peak was not observed in the FCNZ diffraction pattern. Figure 3C shows the hysteresis loops of FCNZ composites annealed at different temperatures. The saturation magnetization (M_s) values of FCNZ-500, FCNZ-600, and FCNZ-700 are 124.8, 138.2, and 164.2 emu/g. The higher M_s value is beneficial in enhancing the magnetization intensity and improving the permeability. Meanwhile, the coercive force (H_c) of FCNZ-500, FCNZ-600, and FCNZ-700 is 2.82, 85.7, and 27.7 Oe, respectively. The difference in H_c may result from the anisotropy of FeCoNi and the defect distribution. Interface-induced magnetic anisotropy is one of the key mechanisms to promote magnetic-dielectric coupling. The presence of $ZnIn_2S_4$ shell layer and its interfacial interactions with FeCoNi core significantly change the magnetic domain structure. The FCNZ-600 samples have a high coercive force (H_c = 85.7 Oe). The enhanced magnetic anisotropy of the FCNZ-600 helps to stimulate and strengthen the magnetic loss mechanism, which is a key process for achieving efficient coupling and dissipation of magnetic energy[38].

To further reveal the composition, XPS analysis was applied on FCNZ-500, FCNZ-600, and FCNZ-700 [Figure 3D-J]. The survey X-ray photoelectron spectra of FCNZ-500, FCNZ-600, and FCNZ-70 indicate that the samples are composed of Fe, Ni, Co, Zn, In, and S elements [Figure 3D]. In the Fe 2p spectrum [Figure 3E], the characteristic peaks of Fe $2p_{3/2}$ and Fe $2p_{1/2}$ and the corresponding satellite peaks can be observed in all samples, indicating different valence states of Fe. The characteristic peak corresponding to 703.8 eV is attributed to Fe^0[39]. Additionally, the peaks observed at 709.9 and 722.9 eV indicate $2p_{3/2}$ and $2p_{1/2}$ of Fe^{2+}, respectively, while satellite signatures at 713.4 and 726.7 eV are associated with Fe^{2+} satellite peaks. Similarly, signals at 711.6 and 723.1 eV correspond to $2p_{3/2}$ and $2p_{1/2}$ of Fe^{3+}, and additional satellite peaks at

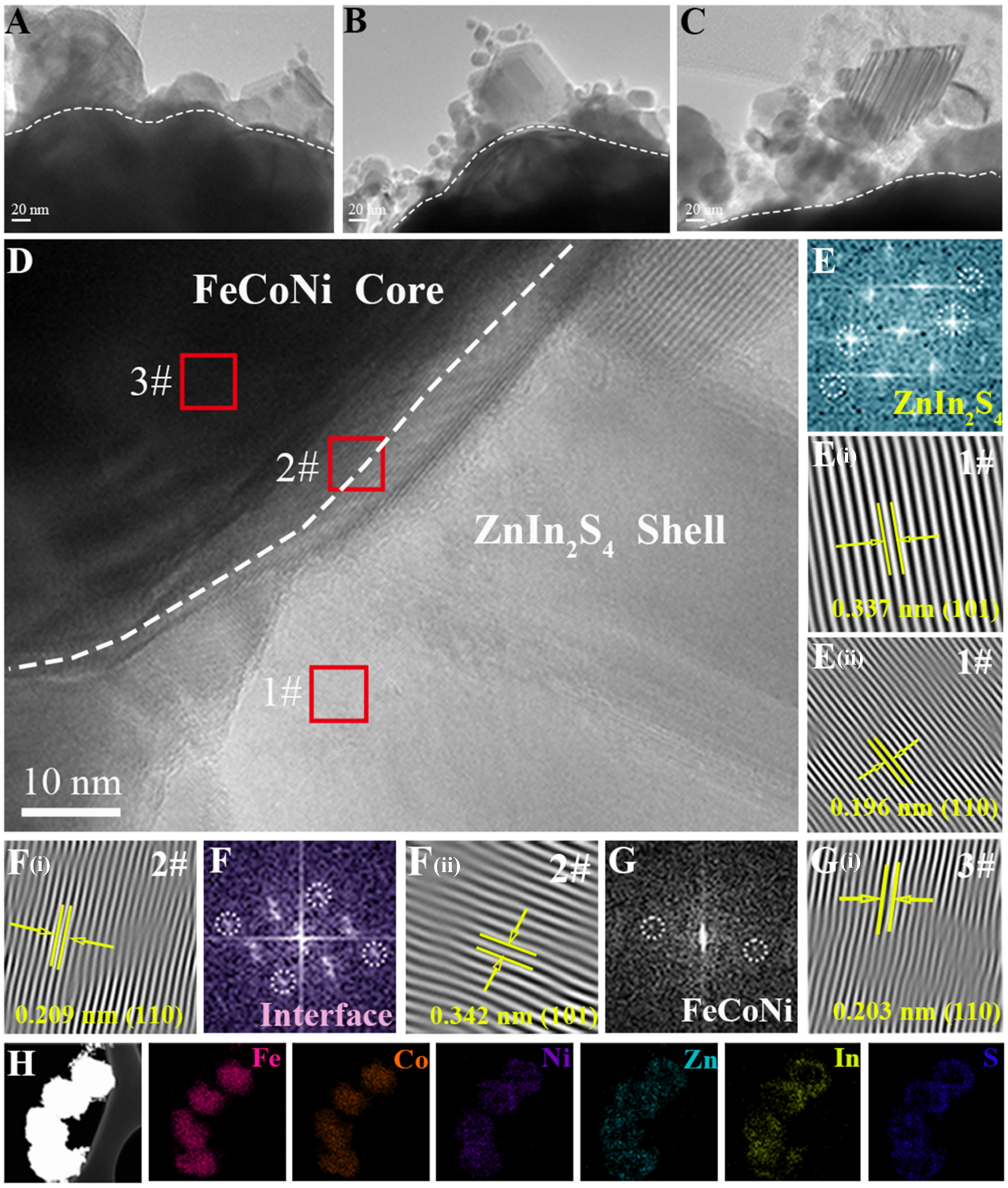

Figure 2. TEM images of (A) FCNZ-500, (B) FCNZ-600 and (C) FCNZ-700; (D) HRTEM image of FCNZ-600; (E-G) FFT patterns corresponding to the red solid frames 1-3; [E(i), E(ii), F(i), F(ii), G(i)] The enlarged image of the region (red solid frame 1-3) in panels (E-G); (H) Element mapping distribution of FCNZ-600. TEM: Transmission electron microscope; HRTEM: high resolution transmission electron microscopy; FFT: fast Fourier transform.

718.4 and 732.2 eV are associated with Fe^{3+}. In the Co 2p spectrum [Figure 3F], the peaks at 778.7 and 793.4 eV represent $2p_{3/2}$ and $2p_{1/2}$ of Co^0, while the signals at 780.9 and 796.7 eV correspond to Co^{2+} $2p_{3/2}$ and $2p_{1/2}$, accompanied by satellite peaks at 785.6 and 802.3 eV[40]. For Ni [Figure 3G], the 2p peaks at 853.1 and 870.2 eV represent $2p_{3/2}$ and $2p_{1/2}$ of Ni^0, while the peaks at 855.9 and 874.3 eV indicate Ni^{2+} $2p_{3/2}$ and $2p_{1/2}$, and the satellite peaks at 861.6 and 878.7 eV are related to Ni^{2+}. Figure 3H shows the Zn 2p spectrum, the peaks at 1,022.0 and 1,044.9 eV are attributed to Zn^{2+} $2p_{3/2}$ and $2p_{1/2}$[41]. In the 3d spectrum [Figure 3I], the signals at 444.7 and 452.3 eV are designated as In^{3+} $3d_{5/2}$ and $3d_{3/2}$. Finally, the S 2p spectrum [Figure 3J] shows S^{2-} $2p_{3/2}$ and $2p_{1/2}$ at the 161.8 and 163.1 eV peak[42]. XPS analysis indicates significant charge transfer and interactions in the interface region.

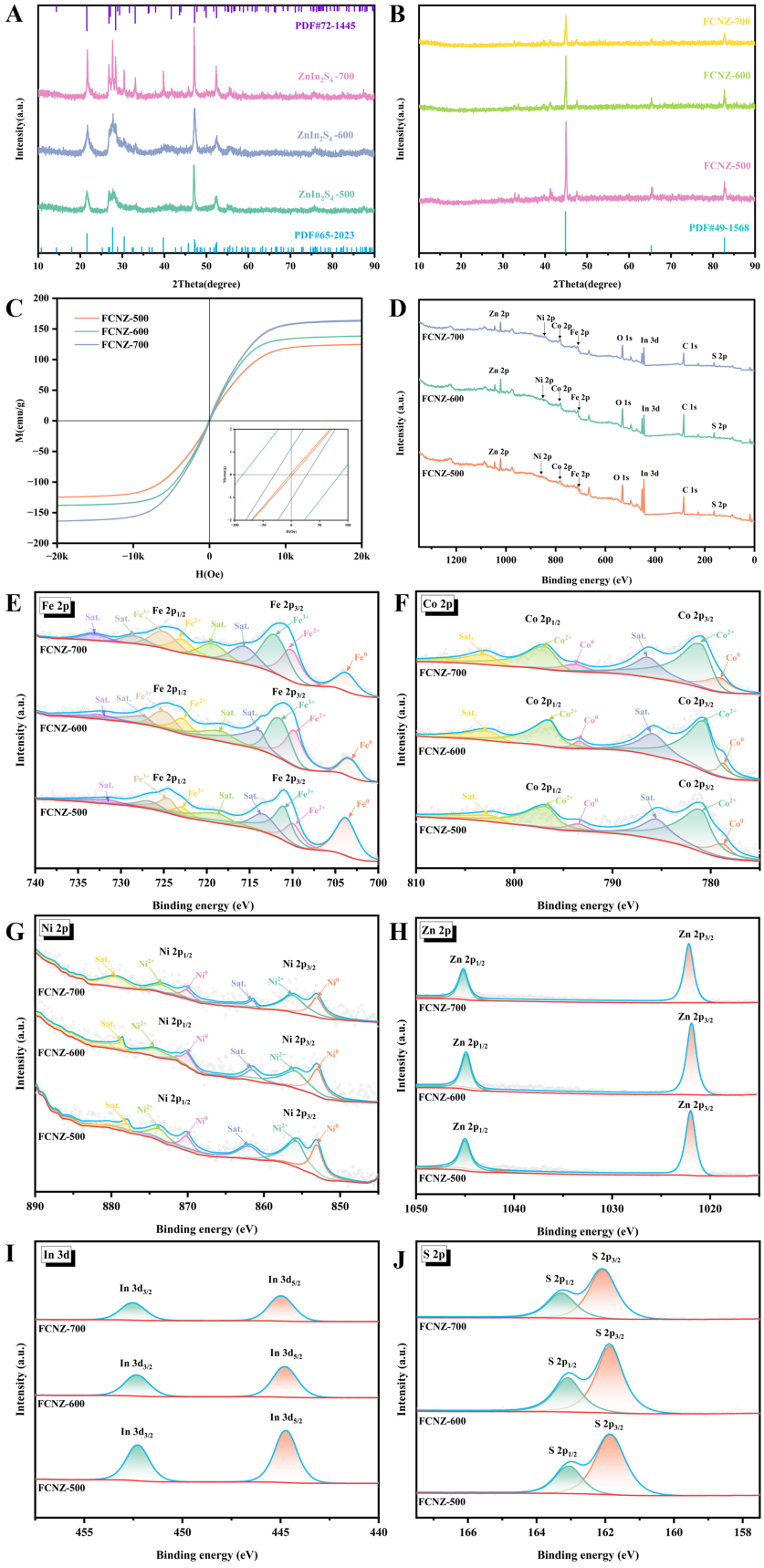
A
PDF#72-1445
$ZnIn_2S_4$-700
$ZnIn_2S_4$-600
$ZnIn_2S_4$-500
PDF#65-2023
Intensity(a.u.)
2Theta(degree)
B
FCNZ-700
FCNZ-600
FCNZ-500
PDF#49-1568
Intensity(a.u.)
2Theta(degree)
C
FCNZ-500
FCNZ-600
FCNZ-700
M(emu/g)
H(Oe)
D
FCNZ-700
FCNZ-600
FCNZ-500
Zn 2p
Ni 2p
Co 2p
Fe 2p
O 1s
In 3d
C 1s
S 2p
Intensity (a.u.)
Binding energy (eV)
E
Fe 2p
$Fe\ 2p_{1/2}$
$Fe\ 2p_{3/2}$
Sat.
Fe^{2+}
Fe^0
FCNZ-700
FCNZ-600
FCNZ-500
Intensity (a.u.)
Binding energy (eV)
F
Co 2p
$Co\ 2p_{1/2}$
$Co\ 2p_{3/2}$
Sat.
Co^{2+}
Co^0
FCNZ-700
FCNZ-600
FCNZ-500
Intensity (a.u.)
Binding energy (eV)
G
Ni 2p
$Ni\ 2p_{1/2}$
$Ni\ 2p_{3/2}$
Sat.
Ni^{2+}
Ni^0
FCNZ-700
FCNZ-600
FCNZ-500
Intensity (a.u.)
Binding energy (eV)
H
Zn 2p
$Zn\ 2p_{1/2}$
$Zn\ 2p_{3/2}$
FCNZ-700
FCNZ-600
FCNZ-500
Intensity (a.u.)
Binding energy (eV)
I
In 3d
$In\ 3d_{3/2}$
$In\ 3d_{5/2}$
FCNZ-700
FCNZ-600
FCNZ-500
Intensity (a.u.)
Binding energy (eV)
J
S 2p
$S\ 2p_{1/2}$
$S\ 2p_{3/2}$
FCNZ-700
FCNZ-600
FCNZ-500
Intensity (a.u.)
Binding energy (eV)

Figure 3. The XRD pattern of synthesized (A) $ZnIn_2S_4$-500, $ZnIn_2S_4$-600 and $ZnIn_2S_4$-700; (B) FCNZ-500, FCNZ-600 and FCNZ-700; the hysteresis loops (C) of FCNZ-500, FCNZ-600 and FCNZ-700; the survey X-ray photoelectron spectra (D) of FCNZ-500, FCNZ-600, and FCNZ-700; high revolution (E) Fe 2p, (F) Co 2p, (G) Ni 2p, (H) Zn 2p, (I) In 3d, (J) S 2p spectra for FCNZ-500, FCNZ-600 and FCNZ-700. XRD: X-ray diffraction.

EM parameters analysis and EM wave absorption performance

The EM parameters predominantly determined the absorption properties. The real parts of permittivity (ε') and permeability (μ') indicate the storage ability of electric and magnetic energy and the imaginary parts of permittivity (ε'') and permeability (μ'') indicate dissipation capability[43,44]. Additionally, $\tan\delta_\varepsilon = \varepsilon''/\varepsilon'$ and $\tan\delta_\mu = \mu''/\mu'$ can be utilized to further analyze the EM wave absorption properties[45].

The values of ε' and ε'' exhibit complex changes and a certain degree of fluctuation. The EM parameters of $ZnIn_2S_4$-500, $ZnIn_2S_4$-600, and $ZnIn_2S_4$-700 [Supplementary Figure 3A-C], ε' and ε'' gradually decrease as the frequency increases. Compared to the low-temperature samples ($ZnIn_2S_4$-500, $ZnIn_2S_4$-600), $ZnIn_2S_4$-700 was annealed at 700 °C in H_2/Ar. This thermodynamically driven process promotes more complete crystal growth, leading to a reduction in defect structures. The lower defect structures enhance electrical conductivity, consequently increasing the complex permittivity of $ZnIn_2S_4$-700 [Supplementary Figure 3A and C]. Interestingly, the incorporation of the magnetic component FeCoNi modifies the internal charge distribution and polarization characteristics, thereby causing a variation in the permittivity. In 2-18 GHz, the ε' values of FCNZ-500, FCNZ-600, and FCNZ-700 decrease from 10.56 to 11.27, 11.41 to 11.99, and 7.88 to 7.80, respectively [Figure 4A]. Compared with the other two samples, FCNZ-600 has higher real permittivity, indicating better energy storage capacity and conductivity. As observed from Figure 4B, the ε'' values vary in the range of 0.30 to 1.96, 0.71 to 1.86, and 0.51 to 0.55 for FCNZ-500, FCNZ-600, and FCNZ-700, respectively. The FCNZ-600 sample exhibits a higher ε'' value, indicating the strongest dielectric loss capability[46]. Compared to FCNZ-500 and FCNZ-700, the FCNZ-600 exhibits an optimized interface structure between the FeCoNi magnetic component and the $ZnIn_2S_4$ dielectric shell, promoting interface polarization. The decrease in the ε'' curve at 11.5-12.5 GHz reflects the natural decay of the dominant interface polarization relaxation process. The ε'' peak in the 10-14 GHz range may be related to the interface between FeCoNi and $ZnIn_2S_4$, the presence of interface can generate interface polarization. In addition, the intrinsic electric dipole moment of $ZnIn_2S_4$ is shifted by the electric field, which triggers the dipole polarization, and the ε'' enhancement of FCNZ-600 is further supported by the optimization of the crystallinity of $ZnIn_2S_4$. FCNZ-600 shows a significant ε'' peak in the 10-14 GHz band [Figure 4B], where the space charge accumulated at the core-shell interface relaxes under the alternating electric field, resulting in the interfacial polarization, and the introduction of FeCoNi significantly alters the interfacial charge distribution and strengthens the polarization strength, thus increasing the ε'' value[47-51]. Both interface polarization and dipole polarization contribute to enhanced dielectric loss. The $\tan\delta_\varepsilon$ is used to characterize loss capability [Figure 4C]. Apparently, in the range of 7.5-9.5 GHz and 13.5-17.5 GHz, FCNZ-600 has relatively higher values of $\tan\delta_\varepsilon$ compared to other two samples, which confirms that FCNZ-600 has a stronger dielectric loss capability.

Compared with $ZnIn_2S_4$ annealed at different temperatures without magnetic properties ($\mu' \approx 1$, $\mu'' \approx 0$, Supplementary Figure 3B), Figure 4D-F respectively shows the μ', μ'', and $\tan\delta_\mu$ curves of the FCNZ-500, FCNZ-600, and FCNZ-700 with FeCoNi magnetic components. The μ' curves of the FCNZ-500, FCNZ-600, and FCNZ-700 show a slowly decreasing trend. The trend of the μ'' curves and the $\tan\delta_\mu$ curves is basically similar magnetic loss capability of the FCNZ-500, FCNZ-600, and FCNZ-700. Furthermore, the average ε' and ε'' values of FCNZ-600, which are the largest compared to FCNZ-500 and FCNZ-700, indicate the good dielectric storage and dissipation capacity [Figure 4G]. Further to this, it is clearly demonstrated that FCNZ-600 exhibits magnetic-dielectric synergy effect.

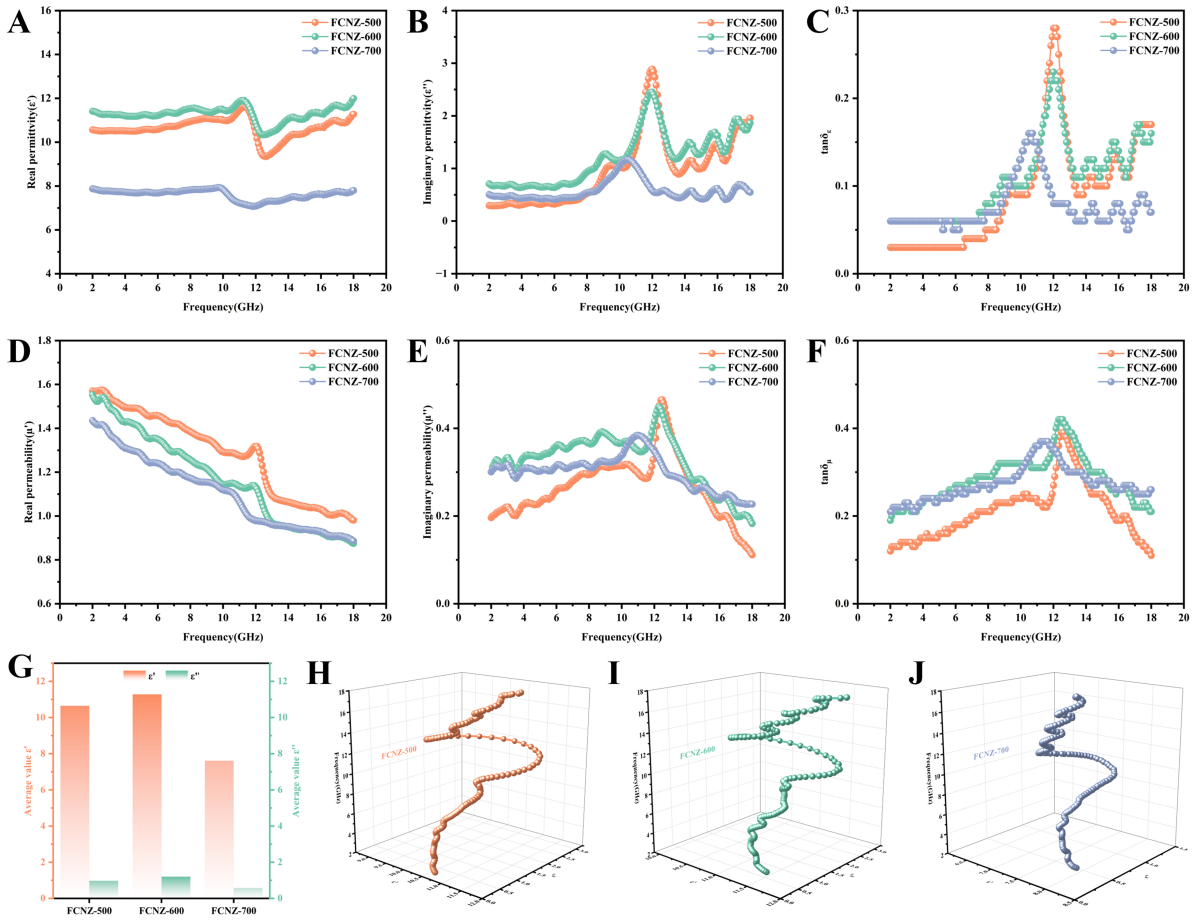

Figure 4. (A) Real permittivity (ε'), (B) imaginary permittivity (ε''), (C) tan δ_{ε}, (D) real permeability (μ'), (E) imaginary permeability (μ''), (F) tanδ_{μ} and (G) average complex permittivity of FCNZ-500, FCNZ-600 and FCNZ-700 composites; Cole-Cole curves of composites of (H) FCNZ-500, (I) FCNZ-600 and (J) FCNZ-700.

The dielectric loss includes the conduction loss and the polarization loss, the relationship between ε' and ε'' can be expressed as[52,53]:

$$\left(\varepsilon' - \frac{\varepsilon_s + \varepsilon_\infty}{2}\right)^2 + (\varepsilon'')^2 = \left(\frac{\varepsilon_s - \varepsilon_\infty}{2}\right)^2$$

One semicircle in the Cole-Cole plot of ε' - ε'' stands for a Debye relaxation process[54]. In Figure 4H-J, FCNZ-500, FCNZ-600, and FCNZ-700 show multiple Cole-Cole semicircles. Meanwhile, interfacial and dipole polarization may exist due to the different electronegativity between atoms[55]. Furthermore, the Cole-Cole curve intuitively reflects that FCNZ-600 has multiple active and distinguishable relaxation processes in wider frequency band.

Based on the complex permeability results, FCNZ-500, FCNZ-600, and FCNZ-700 present good magnetic loss capability. Generally, the magnetic loss is mainly composed of natural, exchange resonance and eddy current loss. By investigating C_0-f - the relationship between the eddy current constant and the frequency - which is further analyzed, the eddy current loss can be evaluated using[54]:

$$C_0 = \mu''(\mu')^{-2}f^{-1} = 2\pi\mu_0 d^2\sigma/3$$

If C_0 maintains a constant value implying that loss originates from eddy current loss, it is clearly observed that the C_0-f curve shows a flat spreading region attributed to eddy current loss within 6-8 GHz; however, the C_0-f curve fluctuates in 2-6 GHz indicating that natural resonance is the main contribution. Meanwhile, the C_0-f curve fluctuates considerably between 8-18 GHz, indicating an exchange resonance at high frequencies [Supplementary Figure 4A].

Also, the attenuation constants α can be utilized for the EM wave absorption performance, as given below[56]:

$$\alpha = \frac{\sqrt{2}\pi f}{c} \times \sqrt{(\mu''\varepsilon''-\mu'\varepsilon')+\sqrt{(\mu''\varepsilon''-\mu'\varepsilon')^2+(\mu'\varepsilon''-\mu''\varepsilon')^2}}$$

The α values of FCNZ-500, FCNZ-600, and FCNZ-700 show a tendency to increase and then decrease with increasing frequency [Supplementary Figure 4B]. In the low-frequency band, the α of the FCNZ-500, FCNZ-600, and FCNZ-700 is weak. In 2-18 GHz, the α value of FCNZ-600 is larger than that of FCNZ-500 and FCNZ-700, indicating that FCNZ-600 has the strongest attenuation ability for EM wave[23].

To study the EM wave absorption performance, the obtained *RL* curves are given in[57]:

$$RL = 20\log|(Z_{in}-Z_0)/(Z_{in}+Z_0)| \quad (1)$$

$$Z = |Z_{in}/Z_0| = \sqrt{|\mu_r/\varepsilon_r|}\tanh\left[j\left(\frac{2\pi fd}{c}\right)\sqrt{\mu_r\varepsilon_r}\right] \quad (2)$$

Based on the corresponding EM parameters, the relevant *RL* intensity and efficient absorption bandwidth (*EAB*) of the obtained FCNZ microspheres were evaluated. Figure 5A-F illustrates the *RL* value curves of FCNZ microspheres, aiming to reveal the relationship between *RL* values and frequency. The RL_{min} values of FCNZ-500, FCNZ-600, and FCNZ-700 are -43.4, -52.4, and -29.2 dB, respectively. Among FCNZ-500, FCNZ-600, and FCNZ-700, FCNZ-600 potentially exhibits the best EM wave absorption performance. At a thickness of 1.9 mm, the RL_{min} value of FCNZ-600 reaches -52.4 dB; meanwhile, at 1.53 mm, the *EAB* of FCNZ-600 can reach 6.08 GHz. Compared with the RL_{min} of $ZnIn_2S_4$ [Supplementary Figure 3D-I], the introduction of FeCoNi magnetic components significantly enhances absorption capability.

Regarding the impedance matching characteristic, when the *Z* value of the material is equal to or extremely close to 1, the EM wave projected onto the material surface can enter the material interior and is almost not reflected[58]. In Figure 5G-I, the impedance matching condition of FCNZ-600 is closer to 1 than FCNZ-500 and FCNZ-700. Therefore, the EM wave projected onto the surface of the FCNZ-600 composite material can enter its interior and be largely attenuated. In addition, the core-shell FCNZ microspheres outperform most of the reported core-shell structured EM wave absorption materials in strong *RL* and wide *EAB* at thin thickness, further confirming the superiority of FCNZ [Figure 5J and K, Supplementary Table 1].

Analysis of EM wave absorption mechanism

Based on the above discussion, excellent core-shell FCNZ-600 is attributed to good impedance matching and multiple electromagnetic wave attenuation mechanisms. The corresponding EM wave absorption mechanism is proposed in Figure 6A. Firstly, under the action of an alternating EM field, at the interface between FeCoNi and $ZnIn_2S_4$ in the FCNZ-600 composite material, due to the difference in EM properties, the charge at the interface will be displaced, forming a polarization current, thereby generating interface polarization loss. At the same time, dipole polarization mainly occurs in the $ZnIn_2S_4$ shell layer[59,60]. The

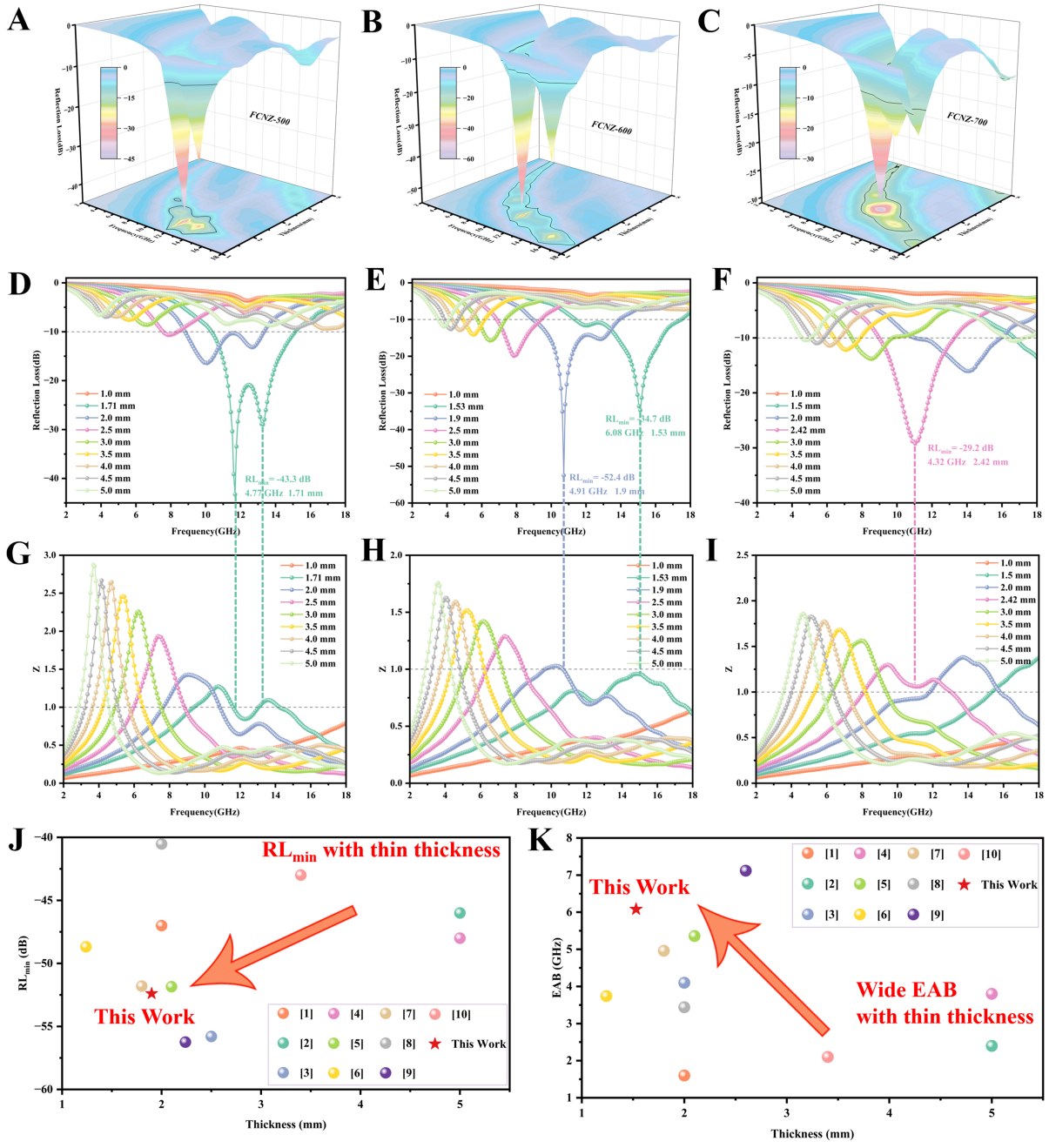

Figure 5. EM wave absorption performance. 3D *RL* diagrams for (A) FCNZ-500, (B) FCNZ-600, (C) FCNZ-700; 2D *RL* diagrams for (D) FCNZ-500, (E) FCNZ-600, (F) FCNZ-700; impedance matching value of (G) FCNZ-500, (H) FCNZ-600, (I) FCNZ-700; (J) RL_{min} and (K) *EAB* comparison between previous reports and this work. EM: Excellent electromagnetic; EAB: efficient absorption bandwidth.

intrinsic electric dipole in the $ZnIn_2S_4$ shell layer undergoes charge displacement and reorientation under the effect of an alternating electric field. At the same time, the high conductivity of FeCoNi core causes an electric field in the $ZnIn_2S_4$ shell layer, which increases the resistance of the dipole to steering and prolongs the relaxation response time, and the free electrons of FeCoNi are injected into the defective sites of the $ZnIn_2S_4$ to increase the interfacial charge density and enhance the polarization strength. The synergistic effect of interfacial polarization and dipolar polarization results in strong dielectric loss capacity, which can

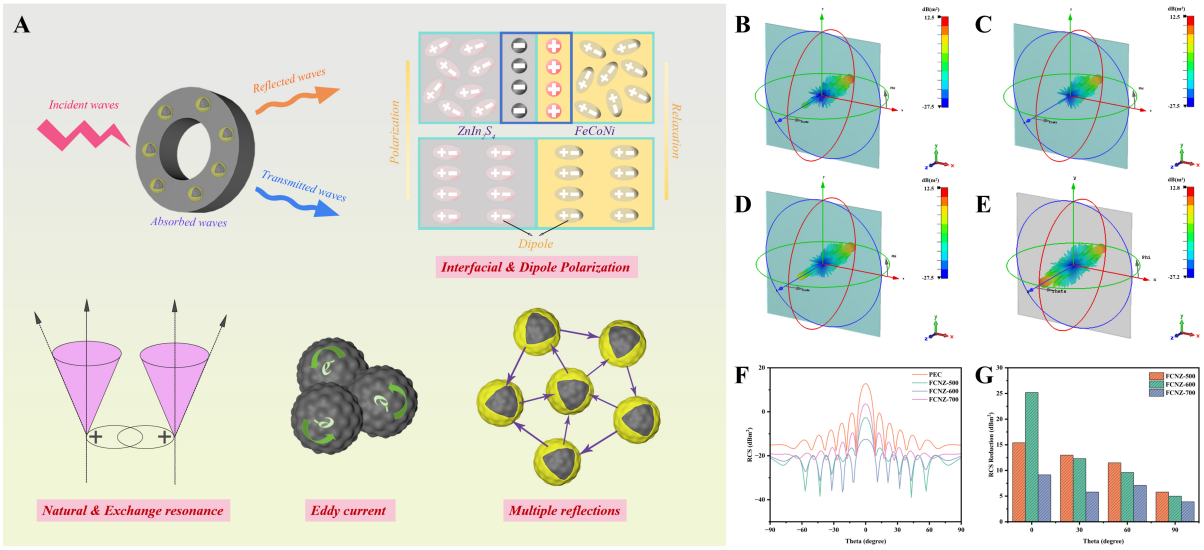

Figure 6. (A) Schematic diagram of the EM wave absorption mechanism of FCNZ-600 composite; 3D RCS images for PEC substrate with (B) FCNZ-500, (C) FCNZ-600, (D) FCNZ-700 coating and (E) no cover; (F) RCS curves at 10.72 GHz and (G) RCS reduction values of FCNZ-500, FCNZ-600, and FCNZ-700. EM: Excellent electromagnetic; RCS: radar cross section; PEC: perfect electric conductor.

more effectively attenuate EM wave energy. Secondly, magnetic loss also plays an important role. FeCoNi gives strong magnetic loss capacity as a magnetic core. The magnetic loss in the FCNZ-600 composite material takes the form of natural resonance, exchange resonance, and eddy current loss. Core-shell FCNZ-600, due to its numerous gaps causing multiple reflections, increases the transmission path of EM wave, which is beneficial to the improvement of attenuation capacity[61].

The effectiveness of the prepared EM wave absorption materials in practical applications was further evaluated using radar cross section (RCS) simulation. The RCS value can be expressed as[62,63]:

$$\sigma(\mathrm{dbm}^2) = 10\log\left[\frac{4\pi s}{\lambda^2}\left[\frac{E_s}{E_i}\right]^2\right]$$

Based on the obtained EM parameters, the performance of FCNZ-500, FCNZ-600, and FCNZ-700 was simulated on a perfect electric conductor (PEC) substrate. The PEC substrate, with dimensions of 180 mm × 180 mm × 10 mm, was coated with 1.9 mm layers of FCNZ-500, FCNZ-600, and FCNZ-700, and the corresponding 3D RCS distributions at 10.72 GHz in Figure 6B-D. In the 3D RCS plot, the PEC substrates coated with FCNZ-500, FCNZ-600, and FCNZ-700 exhibited significantly lower radar wave signals compared to the pure PEC substrates [Figure 6E], indicating effective absorption properties. Among FCNZ-500, FCNZ-600, and FCNZ-700, FCNZ-600 demonstrated the best performance, these simulation results are consistent with the RL_{min} characteristics. Figure 6F depicts the X-band's angle-dependent RCS values at 10.72 GHz. In the range of -90 degrees < theta < 90 degrees, the radar scattering signals of FCNZ-600 are all below -10 dBm^2, which is consistent with its EM wave absorption performance. RCS reduction is compared with PEC at theta = 0, 30, 60, and 90 degrees. Each group contributes differently to the RCS reduction [Figure 6G]. At θ = 0, the RCS reduction of the FCNZ-600 coating is greatest. Based on the simulation results, FCNZ-500, FCNZ-600, and FCNZ-700 effectively reduce radar scattering intensity and confirm their practical feasibility for EM wave absorption applications.

CONCLUSION

In conclusion, the magnetic-dielectric FeCoNi@$ZnIn_2S_4$ system with special core-shell structure was successfully synthesized, which was annealed at different temperatures. These research findings show that when the dielectric shell layer $ZnIn_2S_4$ is introduced and the annealing temperature reaches 600 °C, FCNZ-600 exhibits the RL_{min} of -52.4 dB at 1.9 mm and the *EAB* of 6.08 GHz at 1.53 mm. This is mainly attributed to the synergistic effects among the interfacial polarization between the FeCoNi and $ZnIn_2S_4$ core-shell structures, the dielectric loss, and the magnetic loss. This work demonstrates that the core-shell structure design of magnetic-dielectric synergistic composites is a practical approach for designing high-performance EM wave absorption materials.

DECLARATIONS

Authors' contributions

Project administration, conceptualization, investigation: Sun, R.; Lv, H.; Lian, G.; Huang, M.; You, W.; Wang, L.; Che, R.

Writing - original draft, writing - review and editing: Sun, R.; Wang, L.; Che, R.

Availability of data and materials

Some results of supporting the study are presented in the Supplementary Materials. Other raw data that support the findings of this study are available from the corresponding author upon reasonable request.

Financial support and sponsorship

This work was supported by the National Natural Science Foundation of China (Nos. 52231007, 12327804, T2321003, 22088101, 22405050), the National Key Research Program of China (Nos. 2024YFA1208902, 2024YFA1408000, 2021YFA1200600), the Science and Technology Commission of Shanghai Municipality (No. 24ZR1406400), Aeronautical Science Foundation of China (Nos. 202400180P9001, 2024M0730P9001), Key Laboratory of High Temperature Electromagnetic Materials and Structure of MOE (No. KB202401), Fund of Science and Technology on Surface Physics and Chemistry Laboratory (No. JCKYS2023120201), and Shanghai Municipal Education Commission (No. 24KXZNA06).

Conflicts of interest

Che, R. is Guest Editor of Special Issue "Flexible Materials for Electromagnetic Wave Absorption and Shielding" of the journal *Soft Science*. Che, R. was not involved in any steps of editorial processing, notably including reviewers' selection, manuscript handling and decision making. The other authors declare that there are no conflicts of interest.

Ethical approval and consent to participate

Not applicable.

Consent for publication

Not applicable.

REFERENCES

1. Gao, J.; Ma, Z.; Liu, F.; Weng, X.; Meng, K. Preparation and microwave absorption properties of Gd–Co ferrite@silica@carbon multilayer core–shell structure composites. *Chem. Eng. J.* **2022**, *446*, 137157. DOI
2. Jiang, B.; Shang, J.; Zhang, F.; et al. Electrospinning fabrication of hollow C@TiO_2/Fe_3C nanofibers composites for excellent wave

absorption at a low filling content. *Chem. Eng. J.* **2024**, *495*, 153663. DOI

3. Wei, H.; Li, W.; Bachagha, K. Component optimization and microstructure design of carbon nanotube-based microwave absorbing materials: a review. *Carbon* **2024**, *217*, 118651. DOI
4. Wang, J.; Ren, J.; Li, Q.; Liu, Y.; Zhang, Q.; Zhang, B. Synthesis and microwave absorbing properties of N-doped carbon microsphere composites with concavo-convex surface. *Carbon* **2021**, *184*, 195-206. DOI
5. Rehman, S. U.; Xu, S.; Li, Z.; et al. Hierarchical-bioinspired MOFs enhanced electromagnetic wave absorption. *Small* **2024**, *20*, e2306466. DOI PubMed
6. Habibpour, S.; Rahimi-Darestani, Y.; Salari, M.; et al. Synergistic layered design of aerogel nanocomposite of graphene nanoribbon/MXene with tunable absorption dominated electromagnetic interference shielding. *Small* **2024**, *20*, e2404876. DOI PubMed
7. Wang, B.; Xu, C.; Duan, G.; Xu, W.; Pi, F. Review of broadband metamaterial absorbers: from principles, design strategies, and tunable properties to functional applications. *Adv. Funct. Mater.* **2023**, *33*, 2213818. DOI
8. Wang, X.; Xing, X.; Zhu, H.; Li, J.; Liu, T. State of the art and prospects of Fe_3O_4/carbon microwave absorbing composites from the dimension and structure perspective. *Adv. Colloid. Interface. Sci.* **2023**, *318*, 102960. DOI PubMed
9. Zeng, X.; Cheng, X.; Yu, R.; Stucky, G. D. Electromagnetic microwave absorption theory and recent achievements in microwave absorbers. *Carbon* **2020**, *168*, 606-23. DOI
10. Abdalla, I.; Elhassan, A.; Ali, S.; et al. Impact of defect-rich carbon nanofibers combined with magnetic materials on broadband electromagnetic wave absorption and radar cross-section reduction. *Small. Struct.* **2025**, *6*, 2400624. DOI
11. Cai, L.; Pan, F.; Zhu, X.; et al. Etching engineering and electrostatic self-assembly of N-doped MXene/hollow Co-ZIF hybrids for high-performance microwave absorbers. *Chem. Eng. J.* **2022**, *434*, 133865. DOI
12. Zhang, Y.; Zhu, C.; Gao, S. Multi-scale magnetic and electric interaction in gradient magnetic-dielectric heterostructures with excellent low-frequency electromagnetic wave absorption. *Nano. Res.* **2025**,. DOI
13. An, J.; Zhao, C.; He, Z.; et al. Synthesis and microwave absorption property of nanostructured Ketjen black/Fe_3O_4 core/shell particles. *Rare. Met.* **2022**, *41*, 3351-9. DOI
14. Cui, Y.; Yang, K.; Wang, J.; Shah, T.; Zhang, Q.; Zhang, B. Preparation of pleated RGO/MXene/Fe_3O_4 microsphere and its absorption properties for electromagnetic wave. *Carbon* **2021**, *172*, 1-14. DOI
15. Song, J.; Jiao, J.; Liu, H.; et al. Effect of surface state of SiC fibers on their interfacial properties. *Compos. Commun.* **2025**, *53*, 102232. DOI
16. Meng, X.; Liu, Y.; Han, G.; Yang, W.; Yu, Y. Three-dimensional (Fe_3O_4/ZnO)@C Double-core@shell porous nanocomposites with enhanced broadband microwave absorption. *Carbon* **2020**, *162*, 356-64. DOI
17. He, J.; Gao, S.; Zhang, Y.; Zhang, X.; Li, H. N-doped residual carbon from coal gasification fine slag decorated with Fe_3O_4 nanoparticles for electromagnetic wave absorption. *J. Mater. Sci. Technol.* **2022**, *104*, 98-108. DOI
18. Dong, C.; Li, D.; Wang, H.; et al. $CoSe_2$@polythiophene core-shell composites with enhanced interfacial polarization for high-performance broadband electromagnetic absorption. *Carbon* **2023**, *215*, 118459. DOI
19. Shu, R.; Guan, Y.; Liu, B. Preparation of nitrogen-doped reduced graphene oxide/zinc ferrite@nitrogen-doped carbon composite for broadband and highly efficient electromagnetic wave absorption. *J. Mater. Sci. Technol.* **2025**, *214*, 16-26. DOI
20. Yu, S.; Guo, J.; Zhang, G.; et al. Improved broadband design of SiC/MWCNT absorbing materials through synergistic regulation of heterointerface structure and triple periodic minimal surface meta-structure. *Carbon* **2024**, *226*, 119181. DOI
21. Fan, X.; Xu, Z.; Wang, J.; et al. Constructing magnetic iron-based core-shell structure and dielectric nitrogen-doped reduced graphene oxide nanocomposite for enhanced microwave absorption performance. *Appl. Surf. Sci.* **2023**, *607*, 155013. DOI
22. Chen, J.; Lei, B.; Hou, Y.; et al. Graphene aerogel encapsulated double carbon shell CoFe@C@C nanocubes for construction of high performance microwave absorbing materials. *Carbon* **2024**, *224*, 119081. DOI
23. Zhao, Y.; Zhang, H.; Yang, X.; et al. In situ construction of hierarchical core–shell Fe_3O_4@C nanoparticles–helical carbon nanocoil hybrid composites for highly efficient electromagnetic wave absorption. *Carbon* **2021**, *171*, 395-408. DOI
24. Li, Z.; Zhu, H.; Rao, L.; et al. Wrinkle structure regulating electromagnetic parameters in constructed core-shell $ZnFe_2O_4$@PPy microspheres as absorption materials. *Small* **2024**, *20*, e2308581. DOI PubMed
25. Si, W.; Liao, Q.; Chu, Y.; Zhang, Z.; Chu, X.; Qin, L. A multi-layer core-shell structure $CoFe_2O_4$@Fe_3C@NiO composite with high broadband electromagnetic wave-absorption performance. *Nanoscale* **2023**, *15*, 16381-9. DOI
26. Yang, B.; Fang, J.; Xu, C.; et al. One-dimensional magnetic FeCoNi alloy toward low-frequency electromagnetic wave absorption. *Nanomicro. Lett.* **2022**, *14*, 170. DOI PubMed PMC
27. Huang, M.; Wang, L.; Liu, Q.; You, W.; Che, R. Interface compatibility engineering of Multi-shell Fe@C@TiO_2@MoS_2 heterojunction expanded microwave absorption bandwidth. *Chem. Eng. J.* **2022**, *429*, 132191. DOI
28. Liu, J.; Zhang, L.; Zang, D.; Wu, H. A competitive reaction strategy toward binary metal sulfides for tailoring electromagnetic wave absorption. *Adv. Funct. Mater.* **2021**, *31*, 2105018. DOI
29. Cheng, D.; Xu, J.; Liu, C.; et al. High microwave absorption performance of NiS_2/rGO nanocomposites with a thin thickness. *J. Phys. Chem. Solids.* **2021**, *157*, 110222. DOI
30. Xu, R.; He, M.; Feng, S.; et al. Microstructure optimization strategy of $ZnIn_2S_4$/rGO composites toward enhanced and tunable electromagnetic wave absorption properties. *Dalton. Trans.* **2023**, *52*, 15057-70. DOI PubMed
31. Chaudhari, N. S.; Warule, S. S.; Kale, B. B. Architecture of rose and hollow marigold-like $ZnIn_2S_4$ flowers: structural, optical and photocatalytic study. *RSC. Adv.* **2014**, *4*, 12182. DOI

32. Li, M.; Ren, T.; Li, Y.; et al. Constructing $CdIn_2S_4$/ZnS type-I band alignment heterojunctions by decorating $CdIn_2S_4$ on ZnS microspheres for efficient photocatalytic H_2 evolution. *Int. J. Hydrogen. Energy.* **2023**, *48*, 37224-33. DOI
33. Zhang, C.; Niu, X.; Wei, Y.; et al. $ZnGa_2S_4$: an infrared nonlinear optical material with large second-harmonic generation response and wide band gap. *Rare. Met.* **2024**, *43*, 395-401. DOI
34. Lu, X.; Li, X.; Wang, Y.; et al. Construction of $ZnIn_2S_4$ nanosheets/3D carbon heterostructure with Schottky contact for enhancing electromagnetic wave absorption performance. *Chem. Eng. J.* **2022**, *431*, 134078. DOI
35. Wei, Y.; Wu, Y.; Wang, J.; et al. Rationally designed dual cocatalysts on $ZnIn_2S_4$ nanoflowers for photoredox coupling of benzyl alcohol oxidation with H_2 evolution. *J. Mater. Chem. A.* **2024**, *12*, 18986-92. DOI
36. Li, P.; Zhao, Y.; Zhao, Y.; et al. Trimetallic Prussian blue analogue derived FeCo/FeCoNi@NPC composites for highly efficient microwave absorption. *Compos. Part. B. Eng.* **2022**, *246*, 110268. DOI
37. Li, Q.; Li, X.; Zheng, M.; et al. Spatial coupling of photocatalytic CO_2 reduction and selective oxidation on covalent triazine framework/$ZnIn_2S_4$ core–shell structures. *Adv. Funct. Mater.* **2025**, *35*, 2417279. DOI
38. Shen, J.; Zhang, D.; Han, C.; Wang, Y.; Zeng, G.; Zhang, H. Three-dimensional flower-like FeCoNi/reduced graphene oxide nanosheets with enhanced impedance matching for high-performance electromagnetic wave absorption. *J. Alloys. Compd.* **2021**, *883*, 160877. DOI
39. Xu, X.; Shen, Y.; Jiao, Z.; et al. Improving absorption performance and microstructure of Zr-V-Fe-Co alloys by substitution of Y element for Fe. *J. Mater. Eng. Perform.* **2025**,. DOI
40. Adhikari, A.; Chhetri, K.; Rai, R.; et al. (Fe-Co-Ni-Zn)-based metal-organic framework-derived electrocatalyst for zinc-air batteries. *Nanomaterials* **2023**, *13*, 2612. DOI PubMed PMC
41. Rabchinskii, M. K.; Sysoev, V. V.; Brzhezinskaya, M.; et al. Rationalizing graphene-ZnO composites for gas sensing via functionalization with amines. *Nanomaterials* **2024**, *14*, 735. DOI PubMed PMC
42. Rabchinskii, M. K.; Sysoev, V. V.; Ryzhkov, S. A.; et al. A blueprint for the synthesis and characterization of thiolated graphene. *Nanomaterials* **2021**, *12*, 45. DOI PubMed PMC
43. Yang, K.; Cui, Y.; Liu, Z.; Liu, P.; Zhang, Q.; Zhang, B. Design of core–shell structure NC@MoS_2 hierarchical nanotubes as high-performance electromagnetic wave absorber. *Chem. Eng. J.* **2021**, *426*, 131308. DOI
44. Jiang, X.; Wang, Q.; Song, L.; et al. Enhancing electromagnetic wave absorption with core-shell structured SiO_2@MXene@MoS_2 nanospheres. *Carbon. Energy.* **2024**, *6*, e502. DOI
45. Jiang, R.; Wang, Y.; Wang, J.; He, Q.; Wu, G. Controlled formation of multiple core-shell structures in metal-organic frame materials for efficient microwave absorption. *J. Colloid. Interface. Sci.* **2023**, *648*, 25-36. DOI PubMed
46. Wen, B.; Yang, H.; Lin, Y.; et al. Synthesis of core–shell Co@S-doped carbon@ mesoporous N-doped carbon nanosheets with a hierarchically porous structure for strong electromagnetic wave absorption. *J. Mater. Chem. A.* **2021**, *9*, 3567-75. DOI
47. Wang, X.; Liu, J.; Han, X.; et al. One-dimensional multicomponent nanofibers engineered as heterostructures for electromagnetic stealth applications. *J. Alloys. Compd.* **2025**, *1028*, 180631. DOI
48. Cheng, Y.; Liu, X.; Ren, J.; et al. Component-based modulation engineering to improve magnetoelectric coupling for self-anticorrosion broadband absorption. *Carbon* **2025**, *239*, 120325. DOI
49. Zhu, J.; Cheng, L.; Zhang, S.; et al. 0D/1D hollow heterogeneous structure to induce self-assembly of CNTs for optimized self-anticorrosion and electromagnetic wave absorption performance. *Carbon* **2025**, *238*, 120310. DOI
50. Yu, B.; Jia, Z.; Lv, C.; et al. Antimony-hybridization engineering in p-n heterojunctions for optimized electromagnetic wave absorption. *Small* **2025**, *21*, e2500918. DOI PubMed
51. Zhang, S.; Li, M.; Chen, G.; et al. Achieving high performance microwave attenuation by anchoring magnetic CoNi nanoparticles onto few-layer $Ti_3C_2T_x$MXene. *J. Alloys. Compd.* **2025**, *1023*, 180015. DOI
52. Feng, S.; Wang, H.; Ma, J.; et al. Fabrication of hollow Ni/NiO/C/MnO_2@polypyrrole core-shell structures for high-performance electromagnetic wave absorption. *Compos. Part. B. Eng.* **2024**, *275*, 111344. DOI
53. Han, Y.; Chen, F.; Fu, Q. Heterogeneous three-dimensional FeSiAl@SiO_2@MoS_2 composite with a SiO_2 wave-transmitting layer for enhanced electromagnetic wave absorption performance. *J. Mater. Chem. A.* **2024**, *12*, 25322-33. DOI
54. Zhu, H.; Jiao, Q.; Fu, R.; et al. Cu/NC@Co/NC composites derived from core-shell Cu-MOF@Co-MOF and their electromagnetic wave absorption properties. *J. Colloid. Interface. Sci.* **2022**, *613*, 182-93. DOI PubMed
55. Chang, Q.; Li, C.; Sui, J.; Waterhouse, G. I.; Zhang, Z.; Yu, L. Ni/$Ni_3ZnC_{0.7}$ modified alginate-derived carbon composites with porous structures for electromagnetic wave absorption. *Carbon* **2022**, *200*, 166-77. DOI
56. Li, W.; Li, W.; Ying, Y.; et al. Multifunctional flower-like core-shell Fe/Fe_4N@SiO_2 composites for broadband and high-efficiency ultrathin electromagnetic wave absorber. *J. Mater. Sci. Technol.* **2023**, *132*, 90-9. DOI
57. Zhao, X.; Huang, Y.; Liu, X.; Yu, M.; Zong, M.; Li, T. Magnetic nanorods/carbon fibers heterostructures coated with flower-like MoS_2 layers for superior microwave absorption. *Carbon* **2023**, *213*, 118265. DOI
58. Jiao, Z.; Hu, J.; Ma, M.; et al. One-dimensional core-shell CoC@CoFe/C@PPy composites for high-efficiency microwave absorption. *J. Colloid. Interface. Sci.* **2023**, *650*, 2014-23. DOI PubMed
59. Wu, Z.; Huang, J.; Zeng, X. Dual magnetic particles modified carbon nanosheets in CoFe/Co@NC heterostructure for efficient electromagnetic synergy. *Soft. Sci.* **2024**, *4*, 42. DOI
60. Fan, X.; Zhang, X.; Li, L.; Cao, M. Recent progress and perspective of microwave absorption materials derived from metal-organic frameworks. *Soft. Sci.* **2024**, *4*, 43. DOI

61. Xiao, J.; Zhan, B.; He, M.; et al. Interfacial polarization loss improvement induced by the hollow engineering of necklace-like PAN/carbon nanofibers for boosted microwave absorption. *Adv. Funct. Mater.* **2025**, *35*, 2316722. DOI
62. Rao, L.; Huang, M.; Wang, X.; et al. Atomic infusion induced reconstruction enhances multifunctional thermally conductive films for robust low-frequency electromagnetic absorption. *Angew. Chem. Int. Ed. Engl.* **2025**, *64*, e202418338. DOI PubMed
63. Deng, W.; Li, T.; Li, H.; et al. MOF derivatives with gradient structure anchored on carbon foam for high-performance electromagnetic wave absorption. *Small* **2024**, *20*, e2309806. DOI PubMed